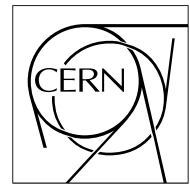


The Compact Muon Solenoid Experiment

CMS Note

Mailing address: CMS CERN, CH-1211 GENEVA 23, Switzerland



September 26, 2007

CMS DT Chambers: Optimized Measurement of Cosmic Rays Crossing Time in absence of Magnetic Field

M. Benettoni, F. Gasparini, F. Gonella, A. Meneguzzo, S. Vanini, G. Zumerle

University of Padova and INFN Padova, Italy

G. Bonomi

University of Brescia and INFN Pavia, Italy

Abstract

Two spare drift chambers produced for the barrel muon spectrometer of the LHC CMS experiment in I.N.F.N. Legnaro Laboratory (Padova, Italy) have been extensively tested using cosmic-ray events. A fitting algorithm was developed to infer in optimal way the time of passage of the particle, from which a timing resolution of $2 ns$ has been obtained. Using cosmic ray data, the algorithm allows to measure the track reconstruction precision of the chambers with the same accuracy as with high energy test beam data.

1 Introduction

Two spare muon drift chambers of MB3 type are being used in the INFN Laboratory in Legnaro (Padova) to assess the feasibility and the limits of the so called muon radiography. This technique uses the multiple scattering of cosmic muons to infer the density of materials contained in closed volumes.

A key requirement of the project is an accurate reconstruction of the muon trajectories before and after crossing the volume under analysis. To this purpose a new fitting procedure of muon tracks crossing a DT chamber has been developed, with the aim of optimizing the time and space resolution in absence of external timing devices. This procedure can be useful to improve the muon track reconstruction and the time of flight measurement in CMS, at least in zones of the chambers where the residual magnetic field is negligible.

All data presented here refer to the chambers MB3-061 and MB3-054, which behaved typically.

2 CMS Detector DT Chambers

The CMS barrel muon detection system [1] consists of 4 concentric shells of wire drift chambers, called MB1 (from the innermost), MB2, MB3, and MB4. They are located on four concentric layers along the beam line inside the five wheels of the iron yoke of the CMS barrel. MB3 chambers were produced in INFN Legnaro National Laboratory during the years 2001-2005.

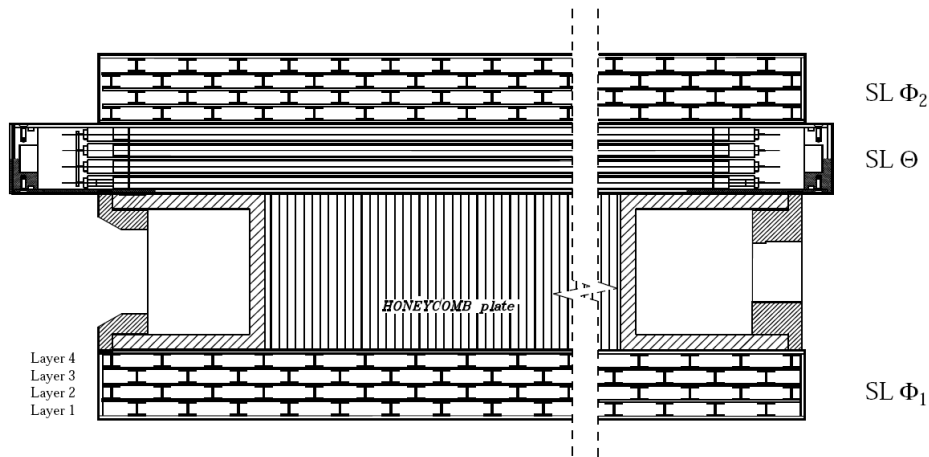


Figure 1: MB chamber cross section.

2.1 Brief Detector Description

A CMS muon chamber [2] consists of 3 independent units, called "Super Layers" (SL), attached to a structural honeycomb support, as shown in Figure 1. Each SL is composed by 4 planes of parallel rectangular drift tubes, called "layers". Each layer is staggered by half cell with respect to the contiguous ones. Two SLs, named SL_{Φ_1} and SL_{Φ_2} , have wires in the same direction. In CMS they measure the muon track position and direction in the bending plane ($\rho - \phi$ plane in the CMS coordinate system). The third SL, named SL_{Θ} , has wires in perpendicular direction and measures the track coordinate parallel to the beam direction.

The cross section of a drift tube is shown schematically in Figure 2. The pitch in a layer is 42 mm . The distance among the wire planes of two consecutive layers is 13 mm . The electric field in the drift cell is shaped by three electrodes: a wire, kept at positive voltage, where the electron multiplication occurs, two cathodes at negative voltage, and two central strip electrodes with voltage intermediate between wire and ground, whose purpose is to improve the field uniformity along the drift path. MB3 chamber wire length is 237.9 cm and 302.1 cm for Φ and Θ SLs, respectively. Each SL_{Φ} contains 286 channels, while the SL_{Θ} contains 227 channels, for a total of 799 channels per chamber. Any charged particle going through a cell volume will generate a signal in its anodic wire. The measurement of the arrival time of the discriminated signal performed by the read-out electronics allows the later reconstruction of the particle track.

The wire signal is processed by the front-end electronics (FE) [4], composed by a fast charge preamplifier (33 ns

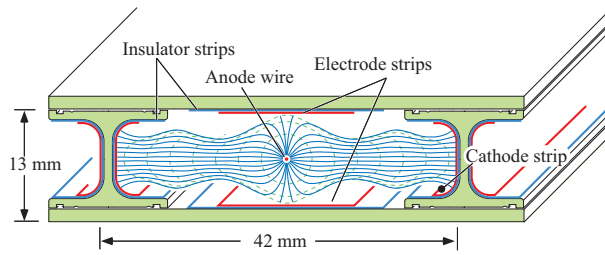


Figure 2: Schematic view of a drift tube. The drift lines (continuous lines) and the isochronous surfaces (dotted lines), computed with the CERN program GARFIELD [3], are also shown.

integration time) followed by a shaper (shaping time 15 ns) and a discriminator. Signals from the front-end electronics are fed into the so-called MiniCrate, an aluminum structure attached to the honeycomb of the chambers, hosting the DT trigger electronics (Trigger Boards - TRB) and the Read-Out Boards (ROBs), together with the necessary services.

The trigger electronics located in the MiniCrate delivers a trigger signal at a fixed time after the passage of a particle. The details of the trigger electronics can be found in [5]. The core of the system is a custom VLSI, called "Bunch and Track Identifier" (BTI). Each BTI reads nine adjacent wire signals in a single SL, and reconstructs the alignment of the signals from the four layers of the SL. The alignment is checked by a sophisticated algorithm called generalized mean-timer method, interpreted roughly as a line fit through the muon chamber planes using the input drift times. An additional device named "Track Correlator" (TRACO) looks for alignment of the track segments of the two SL_{Φ} . The number of aligned hits (3 or 4) in the SL segments and the correlation between the segments of the two Φ SL are used to define a quality flag of the trigger. A third device in the chamber trigger chain, the "Trigger Server" (TS), selects the two best quality tracks in the whole chamber.

The system has been designed for use in LHC, where particles are bunched at the 40 MHz accelerator frequency. The trigger algorithm works on a 40 MHz cycle, and the trigger signal is therefore clocked at the same frequency.

The Read-Out Boards (ROBs) [6] are built around a 32-channel high performance TDC, developed by CERN/EP Microelectronics group.

Neglecting the technicalities of the circuits, the TDC works effectively in common-stop mode, the stop signal being given by the trigger signal. All the wire signals received backwards in time from the stop in a fixed time window, in our case $3.2\text{ }\mu\text{sec}$, are read from the TDC buffers. Each TDC output value is the time from the beginning of the time window to the arrival time of the wire signal, measured in TDC units, equal to $25/32\text{ ns}$.

In standard chamber operating conditions the electrons drift velocity in the cell has approximately a constant value along the full drift path. Therefore, neglecting the small wire-to-wire signal propagation corrections (of the order of the ns), the difference between the TDC times of different wires is directly proportional to the difference of distance of the muon track from the wires. For this reason the TDC raw time histogram, shown in Figure 3, has a box-like shape, commonly called "time-box". The box width, representing the maximum drift time in the cell, is about 400 ns . The tail on the right hand side is due to secondary electrons extracted from the cell walls from UV photons generated by the initial avalanche [7].

To measure the differences of the signal propagation times from FE to ROBs, due to different cable lengths inside the MiniCrate, a common test pulse signal can be injected into each FE amplifier channel. The TDC measurements of the test pulse arriving time is used to correct the TDC output of each channel before data analysis. After this correction, the TDC value for each channel measures exactly the time interval from the TDC time origin to the time at which the signal reaches the FE, within a systematic error that can be estimated to be of the order of 0.5 ns .

2.2 Experimental Setup in Legnaro Laboratory

In the present study, two MB3 chambers were placed horizontally on the cosmic stand in Legnaro. The cosmic ray rate through a chamber is about 800 Hz . Cosmic ray data were collected with the chambers operating in standard conditions as far as gas-mixture, HV settings and discriminator thresholds are concerned. They were filled with an $Ar(85\%) - CO_2(15\%)$ gas mixture, kept at atmospheric pressure (typically $p = 1020\text{ mbar}$), with a gas flow of 0.2 l/min , roughly corresponding to one full gas exchange every 3 days. The standard high voltage values of the cell electrodes were: $V_{wire} = 3700\text{ V}$, $V_{strip} = 1800\text{ V}$, $V_{cathode} = -1200\text{ V}$. At these voltages, and with the

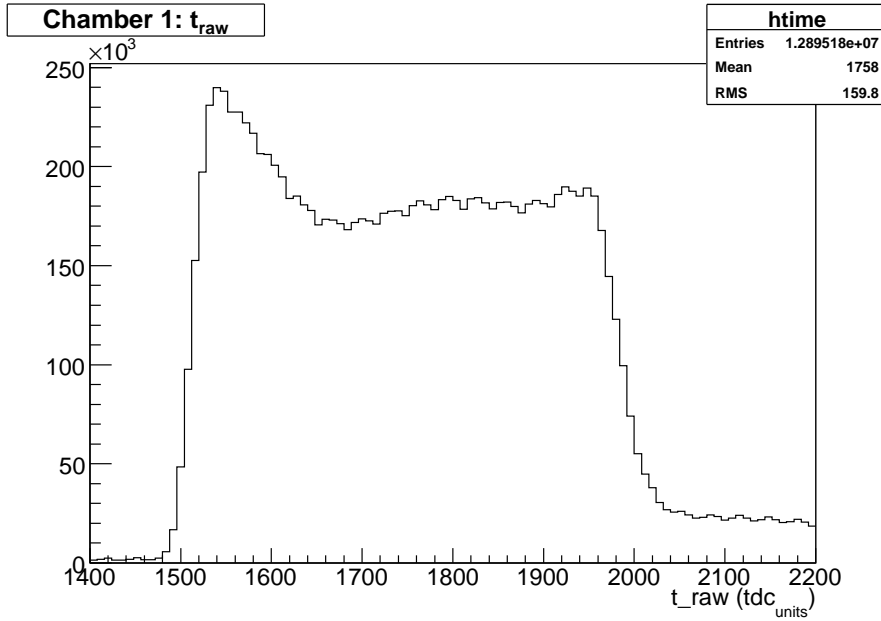


Figure 3: Example of cosmic ray raw time histogram.

gas mixture quoted above, the drift velocity has the approximately constant value of $v_D = 55 \mu m/ns$ along the full drift path [2].

The two chambers have been aligned in the stand with a precision of about $1 mm$, with the wires parallel within $0.5 mrad$. In this way the angles measured in the Φ and the Θ views of the two chambers can be directly compared without off line alignment corrections.

The cosmic stand setup also includes a system of four plastic scintillators, located below the bottom chamber, at a vertical distance of about $1 m$ from it. The time resolution of this system is worse than the intrinsic resolution of the chambers, as obtained with our off line analysis. In addition, the scintillator setup limits the space and angle acceptance of cosmic ray muons. For both reasons we decided not to use the scintillator trigger to collect the data presented in this note, but to use only the trigger issued by the chamber trigger electronics (autotrigger in the following).

3 Cosmic Rays Detection

In this section we will explain in detail the source of the uncertainty on the muon exact crossing time determination, when cosmic rays are detected with CMS muon chambers. The algorithm discussed in this note allows to infer it with the best possible precision, with a final resolution of the order of $2 ns$.

3.1 AutoTrigger Timing with Cosmic Rays

As pointed out in Section 2.1, the TDCs allow the measurement, for each cell, of the time difference between a time origin related to the trigger signal and the time of the signal from the cell. A more detailed treatment is necessary at this point, to understand the relation between the TDC time origin and the time of passage of the particle through the chamber.

The Level 1 trigger signal is not simply issued after a fixed delay from the particle crossing, but after a fixed number of clock cycles following the clock in which the passage of the particle has happened. The TDC time origin in turn is located a fixed number of clock cycles before the Level 1 trigger signal. Therefore there is a fixed number of clock cycles between the TDC time origin and the clock edge immediately preceding the particle passage. Let's call t_{trig} the time of this clock edge, t_μ the time of passage of the muon and t_0 the difference between them: $t_0 = t_\mu - t_{trig}$, so that $t_\mu = t_{trig} + t_0$. From what we just said, the distance in time of t_{trig} from the TDC time origin is the same for all the tracks, and can be determined from the time box distribution, as we shall see in the following. On the contrary, t_0 is different from track to track, its value spanning the range $0 \div 25 ns$.

In CMS, during LHC operation, particles are produced in collisions bunched in time at the same frequency of the clock used in the trigger circuitry. Therefore there is a fixed phase relation between the time at which the muon leaves the interaction point and the clock signal. As a consequence the value of t_0 is calculable using the time of flight of the muon from the interaction point to the chamber and the time t_μ at which the muon crosses a chamber is exactly known for every muon.

This is not true for cosmic rays, that arrive randomly distributed in time. For them t_0 is randomly distributed in the range $0 \div 25 \text{ ns}$ and is not directly calculable. It is one of the purpose of this note to discuss a method to infer the value of t_0 in an optimal way from the measurement of the twelve chamber layers.

From what we just said, t_{trig} can be computed from the known behaviour of the trigger electronics. Alternatively, it can be measured from the time box histogram. This second method allows to automatically take into account the effects of the transit time of signals through cabling and trigger circuitry. Consider muons passing through the wire of a cell. For them the charge amplification occurs without appreciable delay with respect to the particle passage and the time at which their signal arrives to the FE is practically t_μ . Since the signal transit time from FE to ROB is corrected using the test pulse information, as said previously, for these muons the TDC value is equal to $t_\mu = t_{trig} + t_0$. All the other muons, hitting the chamber far from the wires will have TDC values bigger than this, because their signal will be delayed by the drift time of ionization electrons. Since t_0 is randomly distributed in the range $0 \div 25 \text{ ns}$, in the time box histogram t_{trig} is the smallest of all the measured times, the point at which the time box histogram starts.

The purpose of the signal time measurement is to measure the track crossing point using the drift time of ionization electrons, $t_{drift,i} = t_{TDC,i} - t_\mu$ for cell i . Using the trigger information alone, the best approximation of t_μ is $t_\mu = t_{trig} + 12.5 \text{ ns}$. This estimate of drift time suffers from the t_0 intrinsic uncertainty. The r.m.s. of the t_0 distribution is $25 \text{ ns} / \sqrt{12} = 7.2 \text{ ns}$, corresponding to a position error of $\sim 400 \mu\text{m}$ on each layer measurement, completely correlated among the layers. This value has to be compared to the intrinsic resolution of the drift cell, known from test beam measurements to be of the order of $200 \mu\text{m}$.

When fitting a straight line track through the measured hits, the effect of the timing error on the track parameters partially cancels out, as it is evident if the trajectory is such that the wires of consecutive layers lay on opposite sides of the track (see the event display plot in Figure 5 for clarification). However, independently from the size the effect on the track parameters, the residuals from the fitted line will be anyway affected. This has two negative effects:

1. A muon track crossing the chamber layers can produce a δ ray with enough energy to generate ionization electrons far from the muon trajectory. If those electrons are closer to the wire than the muon track, they will produce a signal masking the muon track signal. The measured drift time will be shorter than it should be. The probability for this to happen is $\sim 5\%$ per layer [7]. A fraction of these wrong-measured hits can be eliminated with a cut on the tails of the distribution of the residuals. The broader the distribution, the less efficient will be the cleaning cut.
2. A considerable fraction of the cosmic muons has so low a momentum that the trajectory through the chamber is affected by multiple scattering in a sizeable way. As a consequence, the chamber space precision appears to be worse with cosmic rays than with high energy particles. As we will show in the following chapters, if the residuals of the track fit are not much larger compared to the effect of multiple scattering, it is possible to use the average residual value to select a sample of cosmic muons enriched in the high energy component, recovering the precision obtainable with high energy test beams. The operation is not effective if the residual distribution is too broad.

4 DT Chamber: Local Track Reconstruction

As pointed out in the previous section, it is imperative to determine the exact particle drift times in cells, not affected by the t_0 uncertainty, in order to reconstruct muon tracks obtaining the best track parameters. In this section we will explain the procedure to estimate track parameters with a simple line fit, and the improved algorithm with t_0 estimate.

4.1 Data Sample

The results of this note refer to the analysis of a sample of about a million cosmic ray tracks collected in autotrigger mode. Only events where a single track could be identified in both views of the two chambers were considered for

the analysis.

To measure the particle trajectory, the measured points are fitted with a straight line in both views. In all the fits that will be discussed in the following paragraphs, to reduce the bias from δ rays, hits with a too large residual are rejected. This is done iterating the fit, discarding at each loop the point whose residual from the fitted line is greater than 3σ . The value of σ , for reasons that will be discussed in Section 5.2.2, is chosen to be function of the track angle α in the plane perpendicular to the wire as $\sigma = (250 + 200 \cdot \alpha^2) \mu\text{m}$. The iteration is stopped when all the remaining points lay inside the cut. Events for which less than 6 points are left in the Φ SLs, or less than 3 in the Θ SL, are discarded.

Figure 4 shows the distribution in angle and position of the selected events.

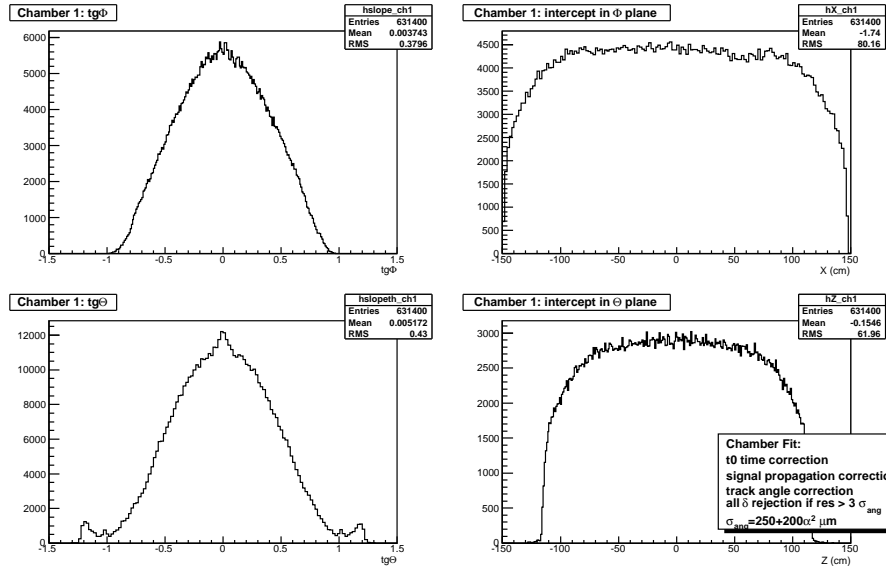


Figure 4: Slope and intercept distributions in Φ and Θ views.

Events are retained for the analysis if $|tg(\Phi)| < 0.8$ and $|tg(\Theta)| < 0.8$.

4.2 Simple Straight Line Fit

The first step in any track reconstruction is the so-called pattern-recognition, where the hits belonging to the same muon track are identified and the left-right ambiguity inherent to any drift chamber is solved (see the event display plot in Figure 5 for clarification).

Thanks to the low flux of cosmic rays, the average time separation between consecutive events is three orders of magnitude larger than the maximum drift time of ionization electrons in a cell. Therefore for most of the events only one track is present, making the pattern recognition a non critical task. We used the pattern-recognition software developed for the official CMS OO-reconstruction program ORCA [8]. The algorithm was adapted to cosmic muon reconstruction simply increasing the measurement error to $\sim 450 \mu\text{m}$, to take into account both the t_0 uncertainty and the possible effects of multiple scattering for low momentum muons. A linear drift space-time relationship inside the cell was assumed, with a uniform drift velocity $v_D = 55.0 \mu\text{m}/\text{ns}$. The algorithm loops over all the possible hit combinations in each SL independently, and in the $2 SL_\Phi$ combined, selecting the best straight line fit, i.e. the one with the biggest number of points and the lowest χ^2 .

A simple straight line fit is therefore used to compute the muon track parameters. The track distance from the wire in cell i is deduced from the drift time ($t_{drift,i}$), assuming linear space-time relationship and using t_{trig} only to estimate t_μ , neglecting the t_0 variation. This simple straight line fit gives broad residuals distributions, as could be seen in Figure 6, where the best estimate of the standard deviation of residuals, $\hat{\sigma} = \sqrt{\sum_i res_i^2 / NDF}$, is plotted.

A very useful quantity to study the drift time measurement precision is the so called Mean Time (MT).

To understand the properties of this quantity, consider first Figure 7. It shows a track passing through a SL,

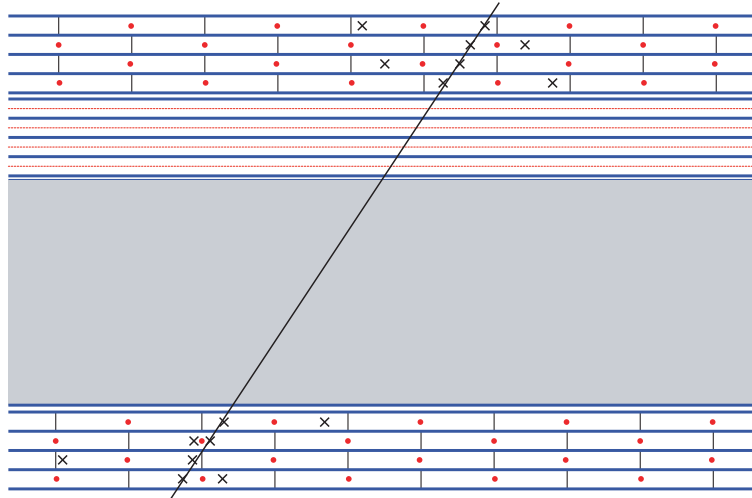


Figure 5: Example of a single event display. The left-right ambiguity of the hits is shown with a cross. Black dots show the position of the wires.

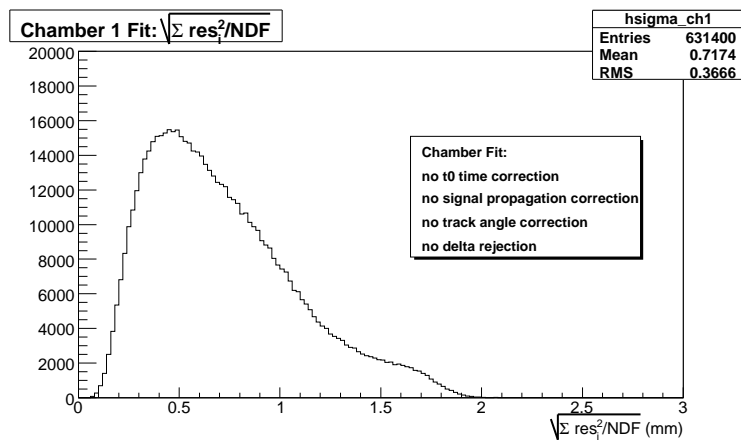


Figure 6: Standard deviation of residuals $\hat{\sigma}$ from simple straight line fit with t_{trig} used as time of passage of the particle.

and contained in a semi-column, the gray region in the figure, composed by four half cells located in the same x coordinate interval. Let d_i be the distances of the track from the wires in the four planes, measured in each wire plane. The following geometrical relations hold:

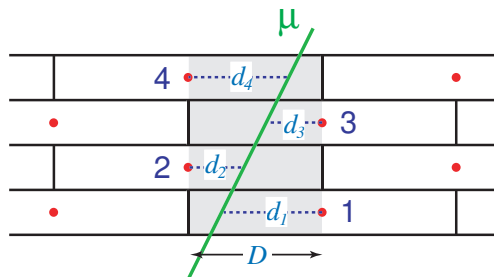


Figure 7: Example of a track completely contained in a semicolumn (the gray area).

$$D = \frac{d_1 + d_3}{2} + d_2 \quad (1)$$

$$D = \frac{d_2 + d_4}{2} + d_3 \quad (2)$$

where D is the width of the semicolumn (half the wire pitch). The relations hold for any angle or position of the track, as long as it is contained in the semi-column. If the space-time relation is linear, similar equations hold for the drift times:

$$MT_{123} = \frac{t_{drift1} + t_{drift3}}{2} + t_{drift2}. \quad (3)$$

$$MT_{234} = \frac{t_{drift2} + t_{drift4}}{2} + t_{drift3}. \quad (4)$$

where the subscripts 123, and 234, indicate the three layers used in the combination. Since the MT value is constant, equal to the time needed to drift across the full semi-column, its experimental width is directly related to the precision of the drift time measurements.

Figure 8 shows the MT distribution when the drift times are computed neglecting the t_0 correction.

The distribution is about 50 ns wide, as expected from the 25 ns uncertainty on t_0 .

The tail visible in the figure on the left side of the peak is due to δ -ray production, as described in section 3.1. To avoid biases, in the following analysis we will always measure the MT average value and resolution fitting a Gaussian function to the peak region of the MT distribution.

4.3 Single Chamber Fit with t_0 estimate

As discussed in previous chapters, if we avoid using t_0 when computing the drift times we introduce an unnecessary large error. Since any error on $t_{drift,i}$ increases the residuals of the track fit, t_0 can be left as a free parameter in the track equation and its value estimated minimizing the χ^2 of the fit.

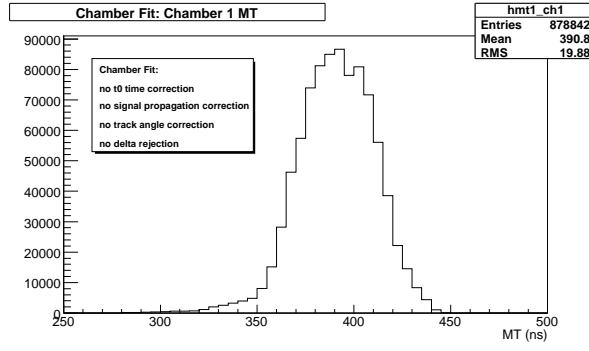


Figure 8: Mean Time distribution when t_{trig} is used as time of passage of the particle on the wire.

This procedure has already been used to analyze cosmic data [9], [10]. The present note carries forward the previous works, extending it to the simultaneous analysis of all the 12 layers of one or several chambers to obtain the best possible determination of t_0 , and therefore the best determination of t_μ .

The trajectory of the particle is described by 2 independent straight lines in Φ and Θ views. The points associated to a track are identified by the coordinates x_i, y_i , in each layer i , where the x coordinate is in the wire plane and orthogonal to the wires, and y is orthogonal to the wire planes. The y_i coordinate is already assumed known from the nominal geometry of the chamber. The x_i coordinate depends on the drift time $t_{drift,i}$ and on the drift velocity v_D . The drift velocity could be left as a free parameter in the track equation and its value and uncertainty estimated minimizing the χ^2 of the fit too (see comment below). Let's define $t_i = t_{TDC,i} - t_{trig}$, where $t_{TDC,i}$ is the raw time read from the TDC channel of wire i . Being $t_\mu = t_{trig} + t_0$, we have $t_{drift,i} = t_{TDC,i} - t_\mu = t_i - t_0$.

We will assume a linear dependence between drift time and muon coordinate in the wire plane, given by the expression:

$$x_i = f_i + \epsilon_i v_D t_{drift,i} = f_i + \epsilon_i v_D (t_i - t_0) = f_i + \epsilon_i v_D t_i - \epsilon_i x_0 \quad (5)$$

where:

- f_i is the nominal x coordinate of the wire where the signal was collected. The chamber construction procedure guarantees that the actual wire position differs from the nominal one by at most $100 \mu m$;
- ϵ_i value is +1 or -1, depending on which side with respect to the wire the track is; ϵ_i is assumed to be known from the preliminary pattern recognition algorithm;
- $x_0 = v_D t_0$. The use of the variable x_0 in place of t_0 simplifies the fit equations.

In the following equations we will use different indexes for the layers of the Φ and Θ views:

- i index is used for the 8 Φ layers. The straight line has equation $x_i = m y_i + a$. The angular coefficient m is 0 for tracks perpendicular to the chamber.
- j index is used for the 4 Θ layers. The line is: $x_j = n y_j + b$.

The χ^2 function to be minimized to find the best lines interpolating the points is:

$$\chi^2 = \sum_i w_i [x_i - (m y_i + a)]^2 + \sum_j w_j [x_j - (n y_j + b)]^2 \quad (6)$$

where $w_i = 1/\sigma_i^2$. The error σ_i should include both the measurement error and the error coming from multiple scattering, if known. In the analysis of this note, since we do not have information on the muon momentum, the multiple scattering contribution cannot be considered on an event by event basis.

Making x_i and x_j dependence from v_D and x_0 explicit, we have:

$$\chi^2 = \sum_i w_i [f_i + \epsilon_i v_D t_i - \epsilon_i x_0 - m y_i - a]^2 + \sum_j w_j [f_j + \epsilon_j v_D t_j - \epsilon_j x_0 - n y_j - b]^2 \quad (7)$$

The variables to be determined by minimizing the χ^2 function are the slopes m, n , the intercepts a, b in the Φ and Θ views, the variable x_0 connected to t_0 and the drift velocity v_D .

The system to be solved is $M\vec{v} = \vec{C}$, where the matrix M is:

$$M = \begin{pmatrix} S_{yy}^i & S_y^i & 0 & 0 & S_{\epsilon y}^i & -S_{\epsilon ty}^i \\ S_y^i & w_i & 0 & 0 & S_\epsilon^i & -S_{\epsilon t}^i \\ 0 & 0 & S_{yy}^j & S_y^j & S_{\epsilon y}^j & -S_{\epsilon ty}^j \\ 0 & 0 & S_y^j & w_j & S_\epsilon^j & -S_{\epsilon t}^j \\ S_{\epsilon y}^i & S_\epsilon^i & S_{\epsilon y}^j & S_\epsilon^j & S_{\epsilon\epsilon}^{i+j} & -S_{\epsilon\epsilon t}^{i+j} \\ S_{\epsilon yt}^i & S_{\epsilon t}^i & S_{\epsilon yt}^j & S_{\epsilon t}^j & S_{\epsilon\epsilon t}^{i+j} & -S_{\epsilon\epsilon tt}^{i+j} \end{pmatrix}.$$

and

$$\vec{v} = (m, a, n, b, x_0, v_D)$$

$$\vec{C} = (S_{fy}^i, S_f^i, S_{fy}^j, S_f^j, S_{f\epsilon}^{i+j}, S_{f\epsilon t}^{i+j})$$

The symbols S_{pqr}^i indicate the sum $\sum_i p_i q_i r_i$.

In this system the drift velocity is left as a fit parameter. However, being v_D the same for all the particles, more precise results can be obtained fixing it to a value determined independently. The modifications of the above equations to use a fixed v_D are straightforward. Except when explicitly quoted, the results shown in the following have been obtained using a fixed value of $v_D = 54.7 \mu m/ns$.

4.4 Two Chambers Global Fit

The method can be extended to any number of layers. A global fit of all the 24 layers (the 2 chambers in sequence) is possible in our setup. In the present note we focused mainly to the single chamber fit, because we want to measure the precision obtained through the comparison of the results of the two chambers. Only as a conclusion of the main goal, in Section 6, we will present some result of a global fit procedure.

As a reference, we give here the equations used in the global fit. An additional couple of indexes for the second chamber Φ and Θ views is introduced:

- k index is used for the 8 planes of chamber 2 SL Φ . The straight line has equation $x_k = py_k + c$.
- l index is used for the 4 planes of chamber 2 SL Θ . The line is: $x_l = qy_l + d$.

The χ^2 function, with v_D and x_0 explicit dependence, this time is:

$$\chi^2 = \sum_i w_i [f_i + \epsilon_i v_D t_i - \epsilon_i z_0 - m y_i - a]^2 + \sum_j w_j [f_j + \epsilon_j v_D t_j - \epsilon_j z_0 - n y_j - b]^2 + \sum_k w_k [f_k + \epsilon_k v_D t_k - \epsilon_k z_0 - p y_k - c]^2 + \sum_l w_l [f_l + \epsilon_l v_D t_l - \epsilon_l z_0 - q y_l - d]^2 \quad (8)$$

We have to find solutions for $M\vec{v} = \vec{C}$, were:

$$M = \begin{pmatrix} S_{yy}^i & S_y^i & 0 & 0 & 0 & 0 & 0 & 0 & S_{\epsilon y}^i & -S_{\epsilon ty}^i \\ S_y^i & w_i & 0 & 0 & 0 & 0 & 0 & 0 & S_\epsilon^i & -S_{\epsilon t}^i \\ 0 & 0 & S_{yy}^j & S_y^j & 0 & 0 & 0 & 0 & S_{\epsilon y}^j & -S_{\epsilon ty}^j \\ 0 & 0 & S_y^j & w_j & 0 & 0 & 0 & 0 & S_\epsilon^j & -S_{\epsilon t}^j \\ 0 & 0 & 0 & 0 & S_{yy}^k & S_y^k & 0 & 0 & S_{\epsilon y}^k & -S_{\epsilon ty}^k \\ 0 & 0 & 0 & 0 & S_y^k & w_k & 0 & 0 & S_\epsilon^k & -S_{\epsilon t}^k \\ 0 & 0 & 0 & 0 & 0 & 0 & S_{yy}^l & S_y^l & S_{\epsilon y}^l & -S_{\epsilon ty}^l \\ 0 & 0 & 0 & 0 & 0 & 0 & S_y^l & w_l & S_\epsilon^l & -S_{\epsilon t}^l \\ S_{\epsilon y}^i & S_\epsilon^i & S_{\epsilon y}^j & S_\epsilon^j & S_{\epsilon y}^k & S_\epsilon^k & S_{\epsilon y}^l & S_\epsilon^l & S_{\epsilon\epsilon}^{i+j+k+l} & -S_{\epsilon\epsilon t}^{i+j+k+l} \\ S_{\epsilon yt}^i & S_{\epsilon t}^i & S_{\epsilon yt}^j & S_{\epsilon t}^j & S_{\epsilon yt}^k & S_{\epsilon t}^k & S_{\epsilon yt}^l & S_{\epsilon t}^l & S_{\epsilon\epsilon t}^{i+j+k+l} & -S_{\epsilon\epsilon tt}^{i+j+k+l} \end{pmatrix}.$$

and

$$\vec{v} = (m, a, n, b, p, c, q, d, x_0, v_D)$$

$$\vec{C} = (S_{fy}^i, S_f^i, S_{fy}^j, S_f^j, S_{fy}^k, S_f^k, S_{fy}^l, S_f^l, S_{f\epsilon}^{i+j+k+l}, S_{fet}^{i+j+k+l})$$

4.5 Drift Time Corrections

The distribution of the standard deviation of residuals $\hat{\sigma}$ after the single chamber fit with t_0 estimate is shown in Figure 9. The Mean Time is shown in Figure 10 as well, computed using the t_0 fitted value.

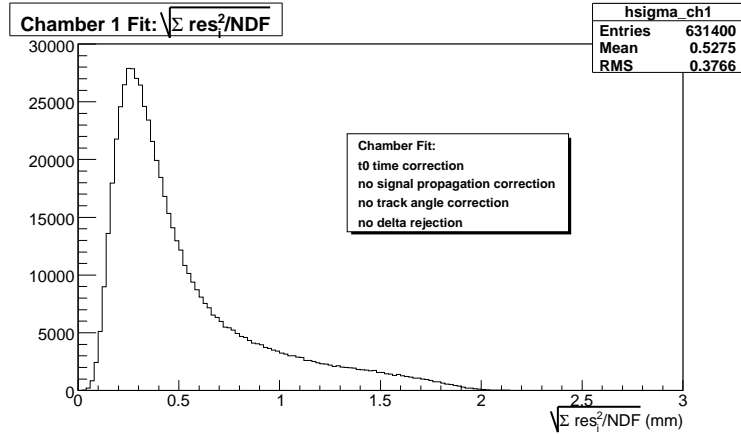


Figure 9: Standard deviation of residuals $\hat{\sigma}$ from straight line fit with t_0 estimate.

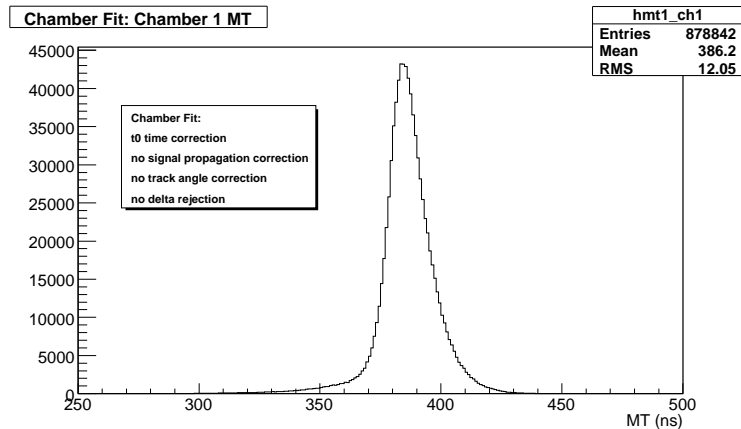


Figure 10: Mean Time for chamber 1 SuperLayers, computed using the t_0 value from the chamber fit.

These figures should be compared with Figure 6 and Figure 8 where the t_0 was not considered in computing t_{drift} . The fit of the t_0 parameter has improved the hit resolution. However, the long tail on the high side of $\hat{\sigma}$ shows that systematic effects are still present.

We can identify two of them:

1. Signal-propagation along the wire: the muon generates an avalanche around the wire in the vicinity of the intersection between the track and the chamber layer. The electric signal propagates then along the wire to the front end discriminator. Since the propagation time depends on the impact point, a correction must be applied event by event.
2. Track angle correction: a linear relationship between the drift time and the coordinate of the track in the wire plane is assumed when deriving the equations used in the fit. This assumption is no longer correct for tracks at large angle of incidence, due to the cell field shape (see the drift and isochronous lines in Figure 2). For large angle tracks, the first ionization electrons arriving to the wire make a shorter path than the electrons released near the wire plane. The delay of the latter depends on the angle of the track but also on the muon

track distance from the wire. We will assume that a large fraction of this effect can be accounted for by a simple shift of the time measurement.

Taking into account those effects, the correct expression for the drift time is:

$$t_{drift,i} = t_i - t_0 - t_{p,i} + t_{\alpha,i} \quad (9)$$

where:

- $t_{p,i}$ is the signal propagation time along the wire from the track crossing point to the FE. It is different in the two Φ and Θ views, but is essentially the same for all the layers in a view,
- $t_{\alpha,i}$ is the phenomenological correction used to take into account the non linearity of the space-time relation for inclined tracks. Again, it is different in the two Φ and Θ views because it depends on the track angle in the plane perpendicular to the wires, but it is the same for all the layers in a view.

Since both $t_{p,i}$ and $t_{\alpha,i}$ are different in the Φ and Θ views, in order to make a simultaneous fit over all the twelve layers we have to correct the measured drift times for those effects. It is useful to remark here that if we limit the fit to one view only, the t_0 parameter in the fit will automatically absorb the t_p and t_α corrections. In this case, the fitted value of the t_0 parameter, that we shall call $t_{0\Phi}$ or $t_{0\Theta}$ depending on the view considered, will be related to the t_0 correction by $t_{0\Phi} = t_0 + t_{p\Phi} - t_{\alpha\Phi}$ in the Φ view, or $t_{0\Theta} = t_0 + t_{p\Theta} - t_{\alpha\Theta}$ in the Θ view. In conclusion, the best t_0 estimate, using the fit over all twelve layers, requires both $t_{p,i}$ and $t_{\alpha,i}$ corrections. In the following subsections we will explain how we evaluated these two corrections.

4.5.1 Signal propagation along the wire

The propagation time along the wire can be measured studying the variation of the MT mean value, as a function of the track impact point position. The Mean Time is a good tool because its width is small, and a variation Δt of $t_{drift,i}$ produces a MT variation twice as big: $\Delta(MT) = 2 \cdot \Delta t$.

We proceed as follows. We fit a straight line through the eight points of the Φ view only, finding the best $t_{0\Phi}$ parameter (we choose the Φ view due to the larger number of layers). This fitted $t_{0\Phi}$, as discussed before, includes the propagation time along the Φ wires. We then use it to compute the Θ drift times for MT_Θ computation.

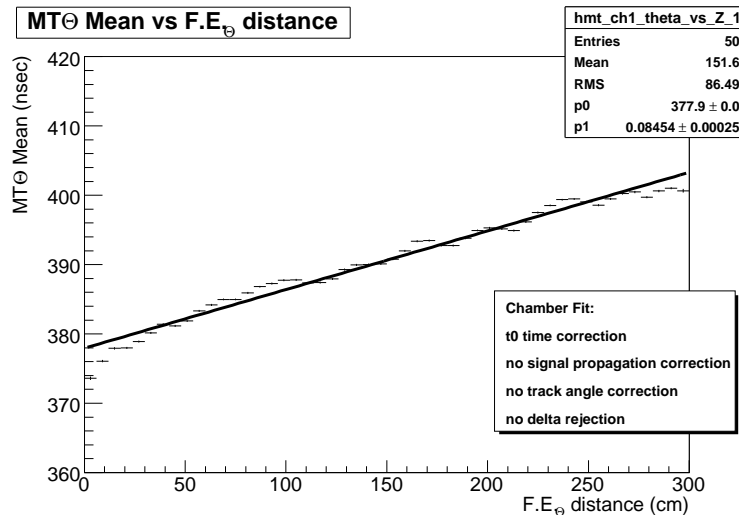


Figure 11: MT_Θ mean value versus distance from Front End Θ , using $t_{0\Phi}$ as t_0 value.

Figure 11 shows the MT_Θ mean value in small intervals of distance from the Θ Front End plotted against the distance. Figure 12 shows the same quantity plotted against the distance from Φ Front End. Since MT_Θ depends on both distances, a more precise measurement of the propagation velocity can be obtained in a plot where the mean MT_Θ is plotted against the difference of the distances from the two front ends. Figure 13 gives this last correlation. Fitting the latter plot with a straight line gives a signal propagation velocity of $v_{prop} = (24.0 \pm 0.1) \text{ cm/ns}$, where the error is statistical only. The value, used in the following analysis, is consistent with the less precise determination reported in [11] and with test bench measurements.

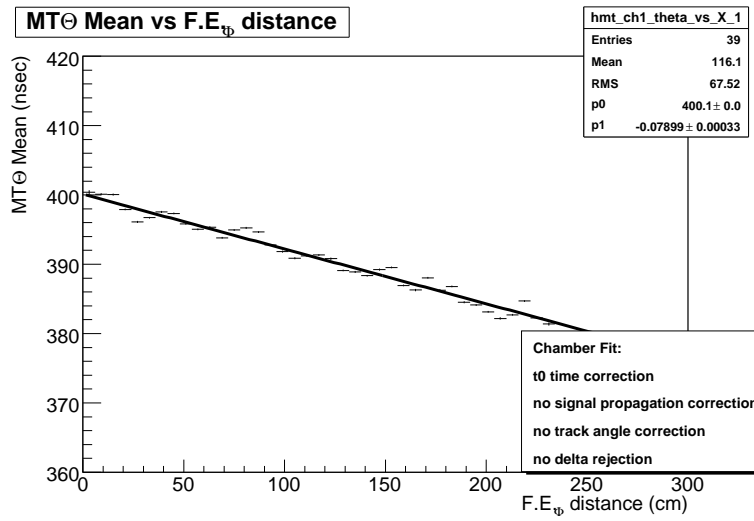


Figure 12: MT_{Θ} mean value versus distance from Front End Φ , using $t_{0\Phi}$ as t_0 value.

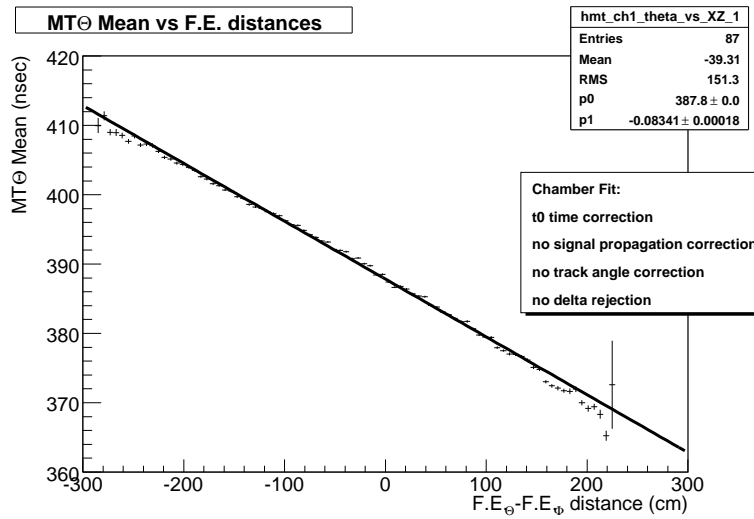


Figure 13: Mean Time Θ versus sum of distances from Front End Φ and Front End Θ , using $t_{0\Phi}$ as t_0 value.

4.5.2 Track Angle Correction

The analysis presented in this section has been done correcting the drift times for the propagation time along the wires, as explained in the previous chapter.

To investigate the effect of the track angle, we first used the MT_Θ variable.

As in the previous paragraph, we fit a straight line through the eight points of the Φ view only and use the fitted $t_{0\Phi}$ to compute the Θ drift times for MT_Θ computation. To limit the analysis to the dependence on the Θ angle, we selected tracks with small angle in Φ view ($|\Phi| < 0.1$). In this way, we are guaranteed that the $t_{0\Phi}$ resulting from the fit is not biased by large Φ angle contributions.

The mean MT_Θ value as a function of Θ is shown in Figure 14. The Mean Time changes by about 8 ns for angles up to 25° . This result is in agreement with the analysis performed previously, see for example [9].

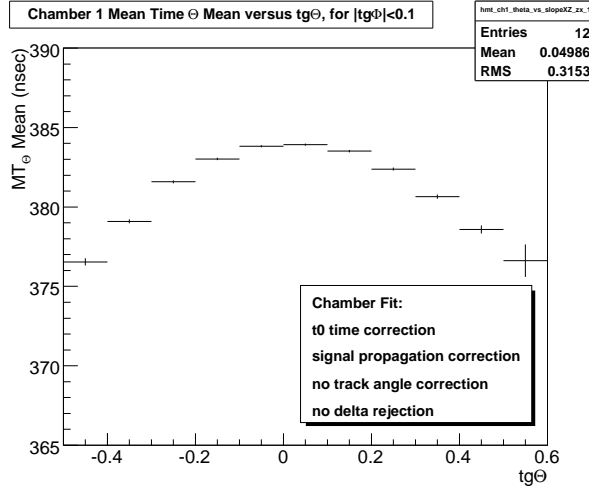


Figure 14: Mean Time Θ versus Θ slope when vertical tracks are selected in Φ view and using $t_{0\Phi}$ as t_0 value.

Unfortunately, the use of the Mean Time restricts the analysis to tracks contained in a semi-column. This constraint biases the distribution of the impact point and limits the track slope to the range $[-0.5, +0.5]$. To extend the analysis to the full angular range of our data sample, and with an unbiased x distribution, we devised a different method. We fit the track in the Θ and Φ view with independent values of t_0 , obtaining the best estimates of $t_{0\Phi}$ and $t_{0\Theta}$. We then study the dependence on the track angle of the difference $\Delta t_0 = t_{0\Phi} - t_{0\Theta}$. Since the propagation time effect is corrected for, we have $\Delta t_0 = (t_0 - t_{\alpha\Phi}) - (t_0 - t_{\alpha\Theta}) = t_{\alpha\Theta} - t_{\alpha\Phi}$.

We first select tracks with a small Φ slope, for which $t_{\alpha\Phi}$ is negligible, so that $\Delta t_0 \approx t_{\alpha\Theta}$. Figure 15 shows how Δt_0 depends on the Θ slope. The shape is almost perfectly parabolic in the full angular range. The same result is obtained choosing tracks with small Θ and plotting Δt_0 against the Φ slope. We expect therefore that for all the events, without any angular cut, the difference Δt_0 will depend on the track angles as $\Delta t_0 = -K \cdot [(tg\Phi)^2 - (tg\Theta)^2]$. This is confirmed from Figure 16. A linear fit to the data of this figure gives for K the value $K = (19.79 \pm 0.04)\text{ ns}$. This value will be used in the following analysis.

5 Analysis of Chamber Fit Results

The full data sample has been reanalyzed applying all corrections discussed so far. All the tracks were fitted in each of the chambers separately, following the method described in Section 4.1. Before the fit, the drift times were corrected for the effects of signal propagation along the wire and for non linearity at large angle, using the preliminary values of impact coordinates and track angles given by the pattern recognition track fit. In this way the t_0 value given by the fit represents the track crossing time for any impact point or angle of incidence of the track.

5.1 t_0 resolution

The main purpose of the fit procedure discussed in this note is to minimize the track position errors by obtaining a precise estimate of t_0 . To measure the precision obtained, the t_0 estimates of the two chambers are compared:

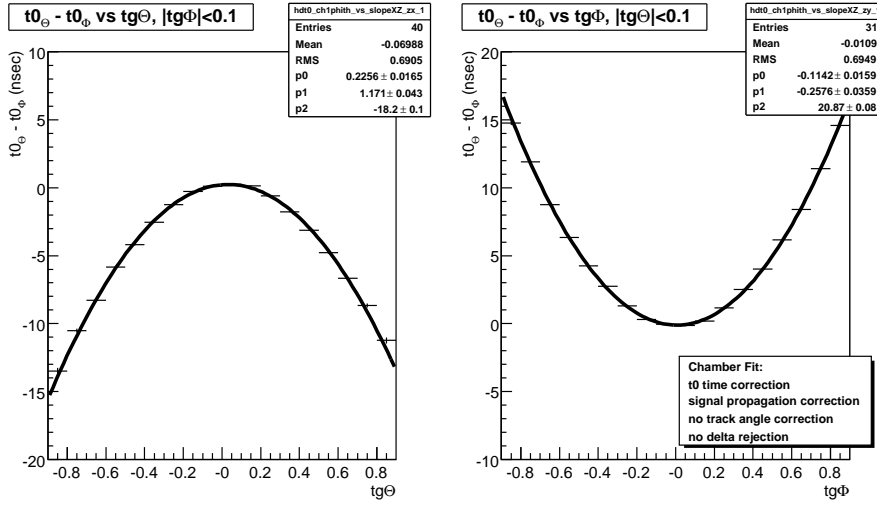


Figure 15: $(t_{0\Theta} - t_{0\Phi})$ versus track slope before angle correction.

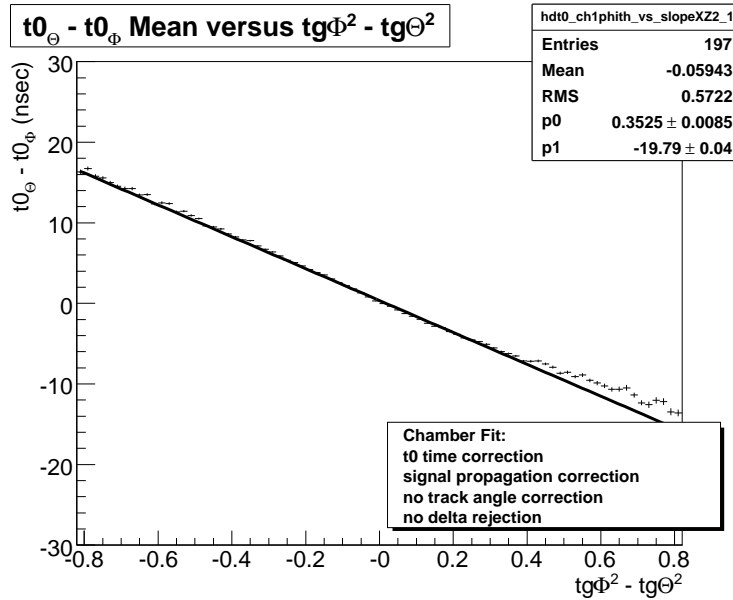


Figure 16: $(t_{0\Theta} - t_{0\Phi})$ versus $[tg(\Phi)^2 - tg(\Theta)^2]$ before angle correction.

Figure 17 shows the histogram of the difference of the two values. The r.m.s. of the distribution is equal to 3.4 ns , from which a t_0 precision of 2.4 ns for the single chamber fit is deduced. Neglecting the tails, the histogram can be fitted by a gaussian function with 2.5 ns width, corresponding to a chamber time resolution of 1.8 ns .

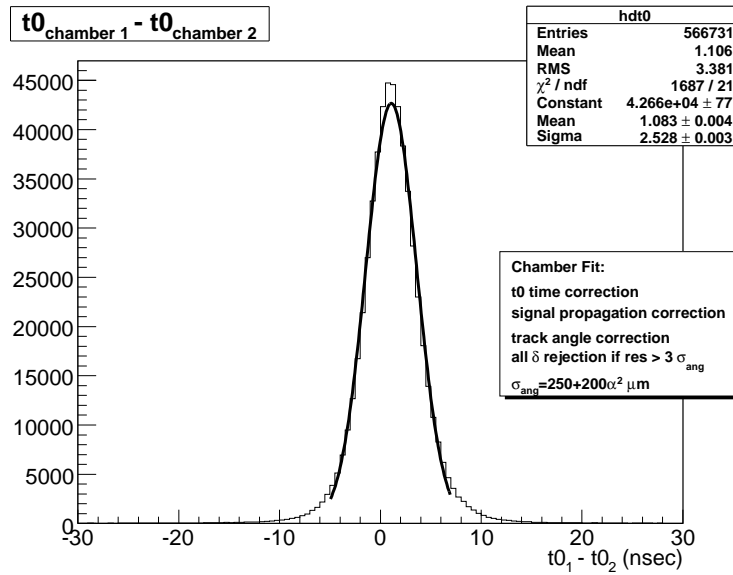


Figure 17: t_0 difference between chamber 1 and chamber 2, all corrections applied.

The average value of the t_0 difference histogram measures the muon time of flight (t.o.f.) from the upper to the lower chamber. The distance h between the middle planes of the two chambers in our stand is $\sim 50 \text{ cm}$, therefore the t.o.f. for vertical tracks is $\sim 1.6 \text{ ns}$, compatible, within the systematic errors, with the measured 1.1 ns .

However, the t.o.f. is expected to vary with the track angle as $h/\cos(\alpha)$, where α is the angle of the track with respect to the vertical. The t.o.f. variation with the track angle is not affected by the systematic uncertainties on the time measurement. Figure 18 gives the average value of the t_0 difference in small intervals of the angle α plotted against $1/\cos(\alpha)$. We observe the expected linear dependence, and the size of the variation is what expected from the relative distance of the two chambers.

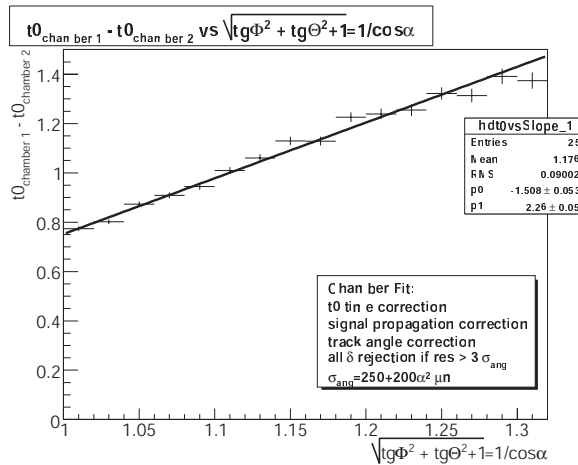


Figure 18: t_0 difference for chamber 1 and chamber 2 versus $1/\cos(\alpha)$.

The good precision of the t_0 determination implies a narrow distribution of the MeanTime variable, as observed in Figure 19.

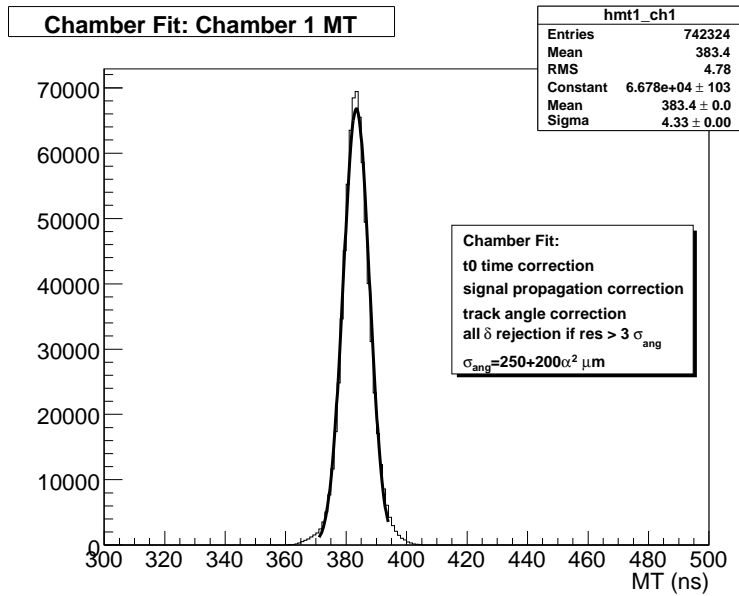


Figure 19: Mean Time Φ , all corrections applied.

5.2 Residuals

The distribution of the standard deviation of residuals of the track fit, $\hat{\sigma}$, is shown in Figure 20. The mean value is now $\sim 300 \mu m$, lower than the value of $530 \mu m$ observed in Figure 9, but still larger than the $\sim 200 \mu m$ observed with test beam data.

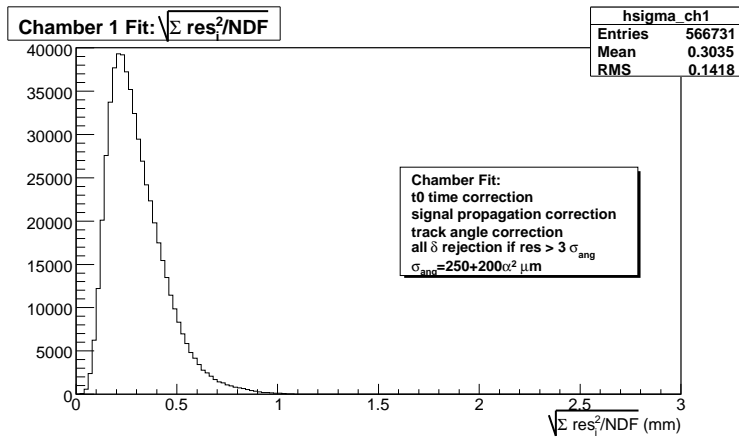


Figure 20: Standard deviation of residuals $\hat{\sigma}$ from straight line fit with all corrections applied.

We can identify two possible sources for this discrepancy:

- The cosmic muons momentum spectrum has a large component of low momentum particles, down to few hundred MeV: in this range the multiple scattering in the chamber material can have a sizeable effect.
- The angular distribution of cosmic ray data is much broader than what is usually considered when taking data in test beams. As discussed in Section 4.5.2, the linearity between drift time and distance of the track crossing point from the closest wire fails for large angle tracks. Therefore we expect larger residuals for large angle tracks.

These hypothesis will be analyzed in the following sections.

5.2.1 Residuals and Muon Momentum

While for high momentum tracks the residuals are essentially due to the measurement errors, residuals for low momentum tracks are expected to be larger, due to the increased multiple scattering of the particle through the chamber material. Therefore, a correlation between the fit residuals in the two chambers is expected, larger for the low momentum component of the spectrum. This correlation is indeed observed in Figure 21 where the distributions of residuals in one chamber are shown for different intervals of the χ^2 value in the other chamber.

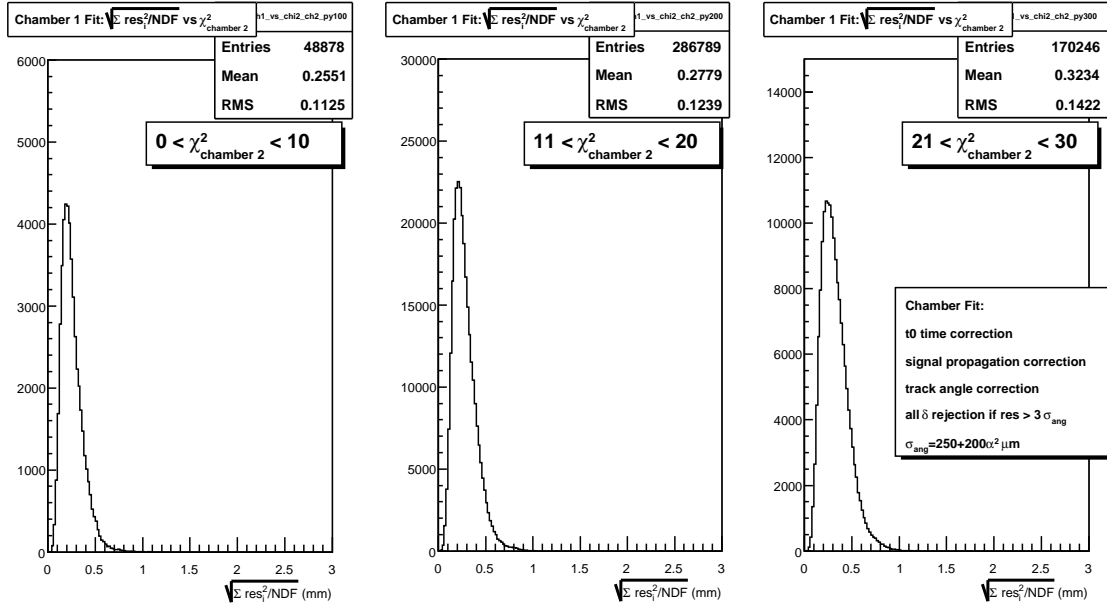


Figure 21: Standard deviation of residuals to the track fit in chamber 1 for different χ^2 ranges of the fit in chamber 2.

Figure 22 shows the standard deviation of residuals distribution for tracks with small Φ and Θ angles ($|\Phi| < 0.2$, $|\Theta| < 0.2$) and small residuals in chamber 2 (chamber 2 $\chi^2 < 15$). The mean value is about $230 \mu\text{m}$, a value not far from test beam data [11].

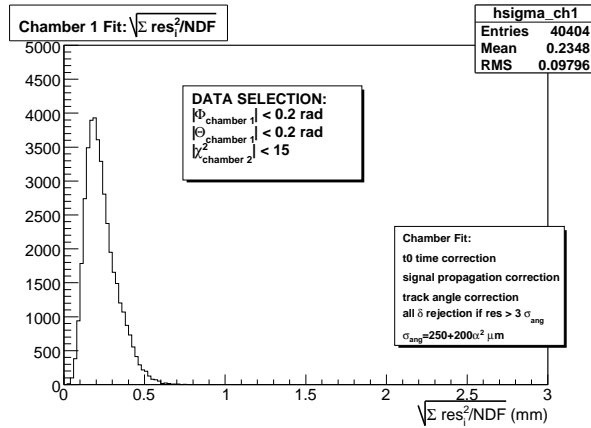


Figure 22: Standard deviation of residuals of chamber 1 fit for small Φ and Θ angles and low χ^2 in chamber 2.

5.2.2 Residuals versus Angle

Figure 23 shows the distribution of residuals in the Φ view for different Φ angle slices. A clear correlation of the width of the distribution with the angle is observed.

To measure the correlation, the data were divided in small Φ slices and the standard deviation of residuals in the Φ view was computed in each Φ bin. The mean value of $\hat{\sigma}$ is plotted in Figure 24 versus the central value of the

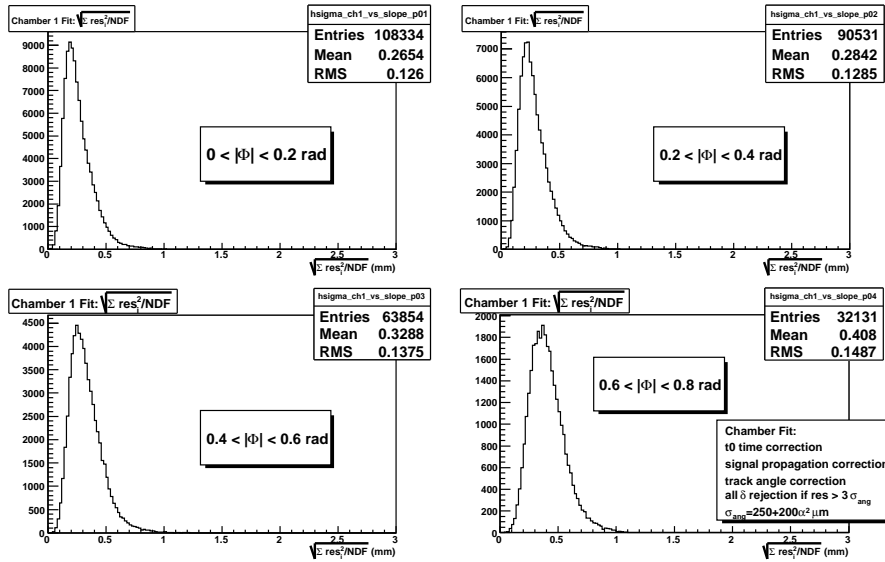


Figure 23: Standard deviation of residuals to the track fit in chamber 1, for different Φ ranges.

Φ interval. An approximate quadratic correlation is displayed. The observed Φ dependence of residuals can be due both to the multiple scattering, since at large angles the particle traverses a bigger thickness of material, and to the non linearity effects of the space-drift time relation. A Monte Carlo simulation, in which the momentum spectrum of the cosmic muons and the materials of the chamber structure have been taken into account, and where the space-drift time relation has been assumed to be linear at all angles, is also shown in Figure 24 with dotted lines. The contribution of the multiple scattering to the increase of residuals appears to be small. The effect of non linearity could be corrected in principle by measuring the exact space - drift time relation as a function of the angle. This further step is outside the scope of this note and will be the subject of a forthcoming work.

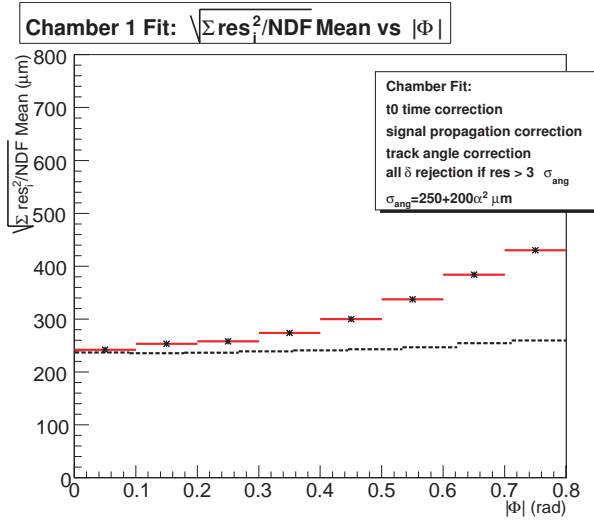


Figure 24: Mean value of the standard deviation of residuals in Φ view, versus Φ angle, compared with MonteCarlo simulation (dotted lines).

5.3 Track Slope Measurement Precision

Being the two chambers well aligned, a comparison of the slopes measured in the Φ and Θ views allows to measure the precision with which the slopes are measured. The Φ slope difference measured in the two chambers is shown in Figure 25. The r.m.s. value of the histogram, in the range $-40 mrad, +40 mrad$ is $9 mrad$, corresponding to a Φ slope precision of about $6 mrad$, much larger than the $mrad$ resolution measured in high energy test beam data [11]. Again this is due to the fact that the cosmic muon momentum spectrum extends to values as low as few

hundred MeV/c. For such muons the multiple scattering can modify the direction of the particle by an angle bigger than measurement resolution. This result is well reproduced by the Monte Carlo simulation quoted in the previous paragraph. The distribution predicted by the simulation is shown as a gray area in Figure 25.

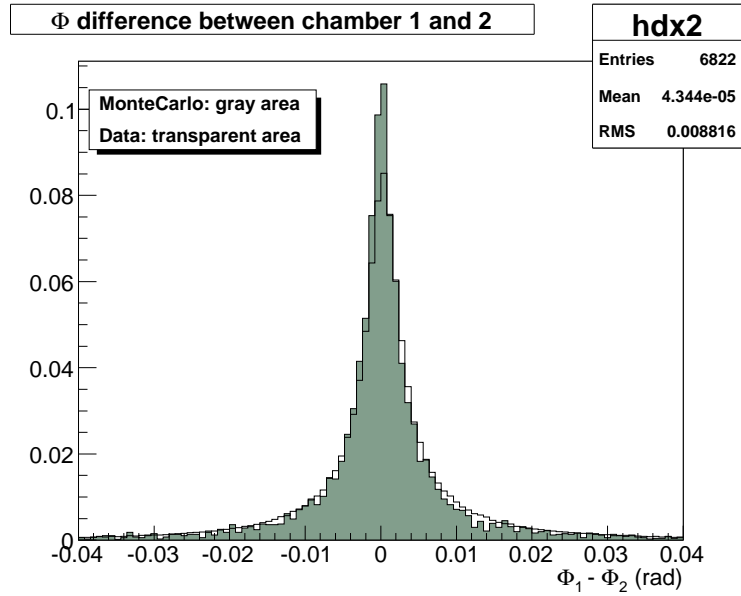


Figure 25: Φ Slope difference between chamber 1 and chamber 2, compared with MonteCarlo simulation.

We can recover the Φ slope precision using again the fit χ^2 in one chamber as a filter to cut the low momentum component of the cosmic ray spectrum. The correlation is clear from Figure 26, where the Φ slope difference histograms are shown for different intervals of chamber 2 χ^2 .

The resolution of the Θ slope, shown in Figure 27, is too big for the effect of multiple scattering to be important.

The fitted slope in the Φ view is much more precise than the one in the Θ view mostly because of the large separation between the two Φ SLs. This large separation has also the positive effect that the slope measurement is less affected by systematic errors deriving from the assumption that the space-drift time relationship is linear. It is therefore interesting to compare the measurement of the Φ angle obtained with one single Φ SL, called ϕ_1 or ϕ_2 in the following, and the one obtained with both SLs (ϕ_{12}). To look for systematic effects, data were divided in bins of ϕ_{12} , and the $\Delta\phi = \phi_{12} - \phi_1$ distribution of each sample was fitted with a gaussian function. Figure 28 shows the mean value and the width of the gaussian function plotted versus the central value of the ϕ_{12} interval for chamber 1. No systematic effect is visible, apart from a slight increase of the width for the larger angles. The small shift from zero of the mean value is compatible with the construction alignment precision of the layers inside a SuperLayer, better than $100 \mu m$.

This result guarantees that the angle measurement in the Θ view, obtained with one superlayer only, is not affected by significant systematic biases.

The same analysis was repeated in chamber 2. The absence of bias could be observed there only after having increased the distance between the two Φ SL by $1.5 mm$ with respect to the nominal value. We verified a posteriori that the honeycomb panel of this chamber had been built outside tolerance, and the thickness was $1.5 mm$ larger than the design value. This shows that the measurement of cosmic ray tracks can be a powerful tool to spot and correct construction anomalies of the chambers.

5.4 Fit of the drift velocity

As already said, all the results presented until now have been obtained fixing the drift velocity value to $v_D = 54.7 \mu m/ns$. On the same data sample, a fit with the drift velocity left as free parameter was also performed. Figure 29 shows the value of the velocity given by the fit in each of the two chambers. The average value in the two chambers are very close and consistent with the value we used in the fits with v_D kept fixed. The r.m.s. of the distribution is $\sim 4\%$. This is the precision with which a single track can measure the effective drift velocity, if we assume that it is the same in all the layers.

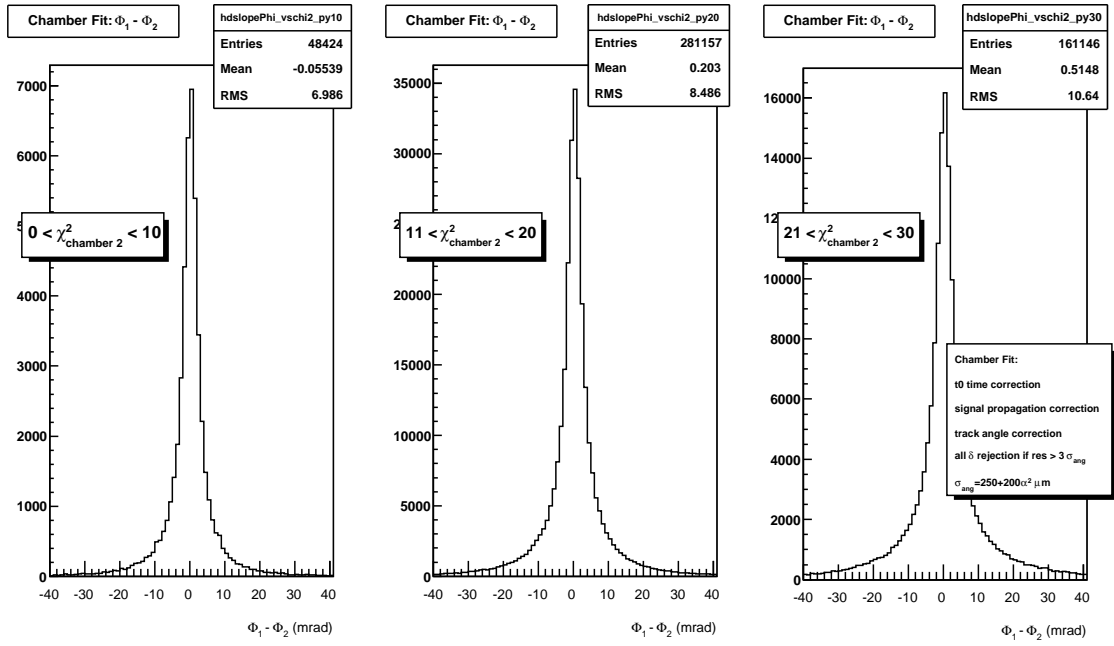


Figure 26: Φ Slope difference for different chamber 2 χ^2 slices.

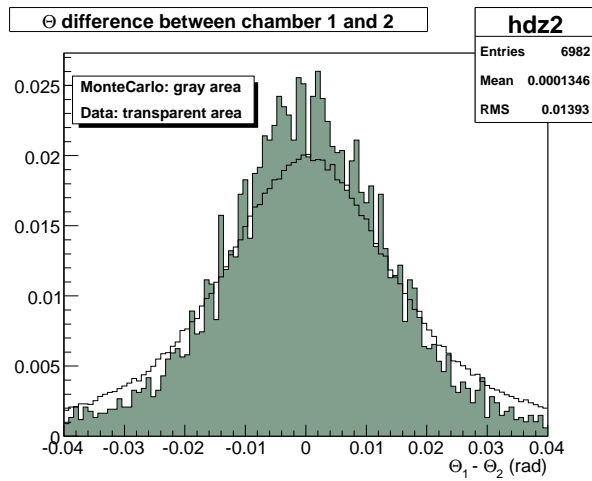


Figure 27: Θ Slope difference between chamber 1 and chamber 2, compared with MonteCarlo simulation.

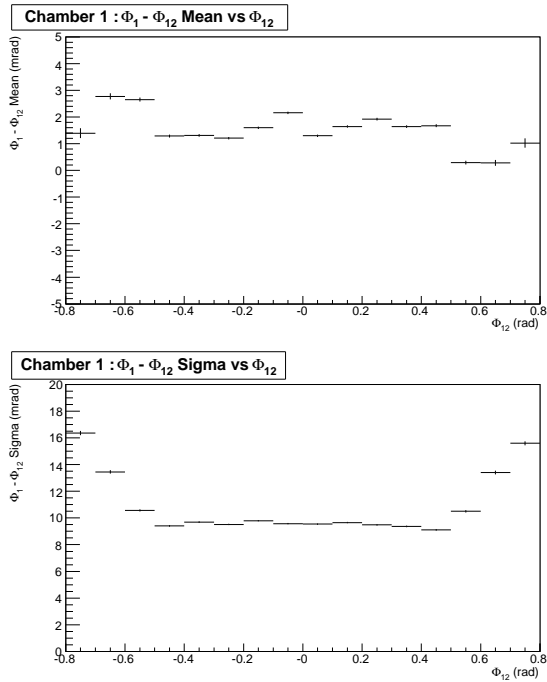


Figure 28: Difference $\Delta\Phi = \phi_{12} - \phi_1$ plotted against the slope (see text for the meaning of symbols). Top: Mean value of $\Delta\Phi$ versus Φ . Bottom: Sigma of $\Delta\Phi$ versus Φ .

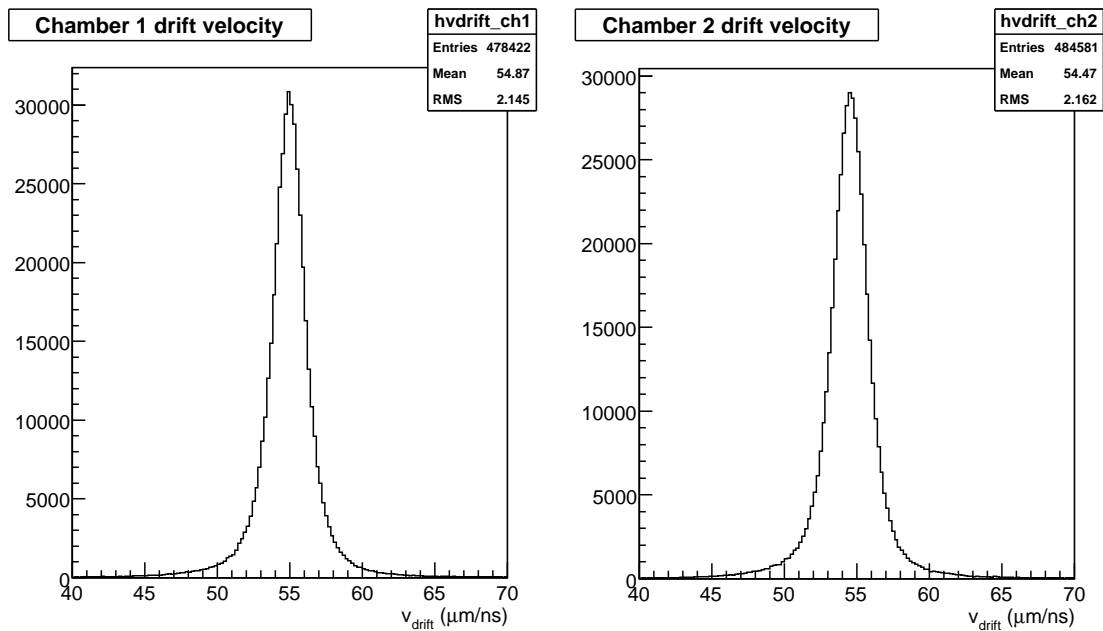


Figure 29: Fitted drift velocity in chambers.

6 Global Fit Results

A simultaneous fit to both chambers is expected to reduce the error on t_0 by a factor $\sqrt{2}$, from 2.4 ns to about 1.7 ns .

We expect to observe the presence of such a small effect (from $130 \mu\text{m}$ to $90 \mu\text{m}$ in space) only in events with the best resolution. Figure 30 shows the Φ slope difference histograms for different intervals of chamber 2 χ^2 . This figure has to be compared with 26, where the same quantity was plotted, but compute fitting the two chambers independently. The improvement is present, more important for low χ^2 . We cannot say if the global fit improves the precision of the angle measurements, or if the decrease of the t_0 error contribution on the residuals improves the momentum selection operated by the χ^2 cut.

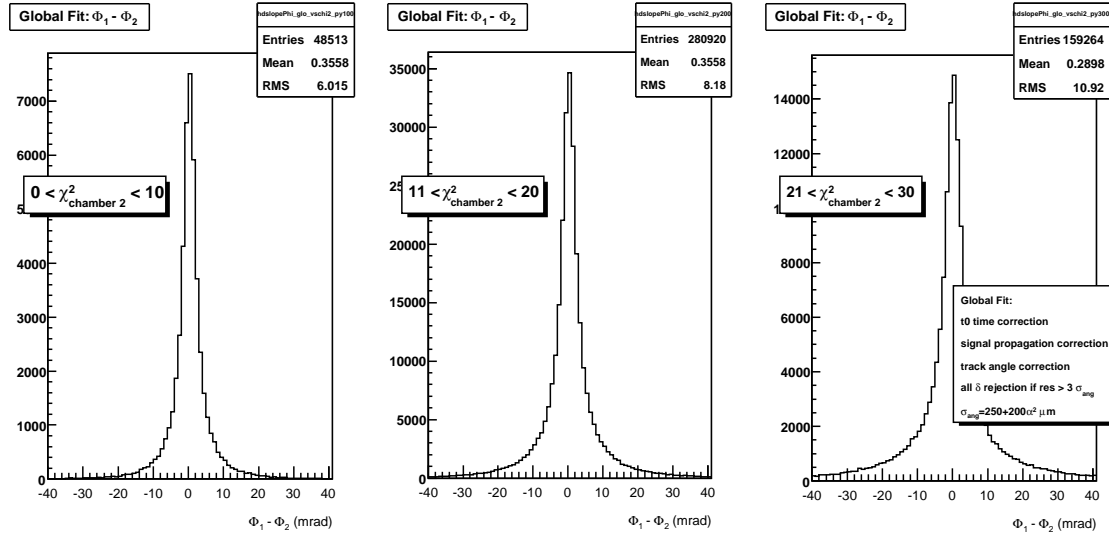


Figure 30: Slope difference for different chamber 2 χ^2 slices.

7 Conclusions

Two MB3 chambers assembled in the INFN production center at Legnaro have been extensively studied using the cosmic ray test facility which was set up in Legnaro to test the chamber behavior. The analysis was used to develop and check a fitting procedure to find the best timing precision of muon crossing the two chambers, in absence of external timing devices.

A timing precision from a single chamber of 2.4 ns has been observed. Selecting tracks with low χ^2 in a chamber allows to select a sample of muons of momentum large enough that the resolution of the other chamber can be measured with the same precision as observed in high energy test beams, with a uniform illumination of the chamber and a large angular spread of the particles crossing the chamber.

References

- [1] “The CMS muon project, CMS Technical Design Report”, CERN/LHCC 97-32, CMS TDR, december 1997.
- [2] M. Aguilar-Benitez et al., “Construction and test of the final CMS Barrel Drift Tube Muon Chamber prototype”, Nucl. Instrum. Meth. A **480** (2002) 658
- [3] R. Veenhof, “GARFIELD. Simulation of gaseous detectors”, CERN Writeups, Ref. W5050.
- [4] M. Cavicchi, F. Gonella, I. Lippi, P. Guaita, M. Pegoraro, E. Torassa, “Properties and Performances of a Front-end ASIC Prototype for the Readout of the CMS Barrel Muon Drift Tubes Chambers”, CMS Note 1999/033.
- [5] CMS Collaboration, “Level-1 Trigger Technical Design Report”, CERN LHCC 2000-038.
- [6] C. Fernandez Bedoya, J. Marin, J. C. Oller and C. Willmott, “Electronics For The Cms Muon Drift Tube Chambers: The Read-Out Minicrate”, IEEE Trans. Nucl. Sci. **52** (2005) 944

- [7] M. Benettoni *et al.*, “*Performance of the drift tubes for the barrel muon chambers of the CMS detector at LHC*”, Nucl. Instrum. Meth. A **410** (1998) 133.
- [8] *The Object Reconstruction for CMS Analysis program (ORCA)*, <http://cmsdoc.cern.ch/orca/>.
- [9] F.R. Cavallo *et al.*, “*Test of CMS Muon Barrel Drift Chambers with Cosmic Rays*”, CMS Note 2003/017.
- [10] M. Benettoni *et al.*, “*Study of the Internal Alignment of the CMS Muon Barrel Drift Chambers using Cosmic Rays Tracks*”, CMS Note 2004/001.
- [11] C. Albajar *et al.*, “*Test beam analysis of the first CMS drift tube muon chamber*”, Nucl. Instrum. Meth. A **525** (2004) 465-484.